東京大学 大学院新領域創成科学研究科
基盤科学研究系物質系専攻

平成 18 年度
修士論文

Nanostructure growth on termination-controlled $SrTiO_3$ surfaces

終端面を制御した $SrTiO_3$ 上のナノ構造成長

2007 年 1 月 30 日提出
指導教員： Mikk Lippmaa 助教授

56118

Hiromasa Kondo

Nanostructure growth on termination-controlled $SrTiO_3$ surfaces

Contents

Chapter 1
General Introduction

1-1 Introduction

Much of the technological development in the latter half of the 20th century can be attributed to a rapid progress in silicon-based semiconductor electronics. Nowadays, large-scale integrated circuits can be found in almost all electronic instruments, resulting in dramatic advances in industry, biology, medical science, and so on.

However, limitations of silicon as a foundation for electronics are well known and the limitations are beginning to be felt in practical applications, such as high-speed digital devices, low-power devices, and in high-density storage. As a solution, attention has turned to enhancing device performance by applying new materials, eventually replacing silicon. In case of traditional semiconductors, applications are limited because it is 'only' possible to make use of a single degree of freedom, namely electric charge. In contrast, materials like transition metal oxides have several degrees of freedom. In addition to electrical charge, it is possible to utilize spin and orbital order. These forms of order are exhibited as a wide range of useful physical properties, such as high-T_c superconductivity in cuprates[i] or colossal magnetic resistance in manganites[ii]. It may be expected that the next generation of electronic devices will utilize these types of effects and it is for this reason that I have investigated the transport properties of perovskite oxide nanostructures.

The perovskite structure (ABO_3) is shown in Fig. 1-1. The unit cell of ABO_3 is represented by the A-site ions at the body center and the B-site ions at the corners. Oxygen atoms form octahedra that surround the B-site ions. The diverse physical properties of perovskites are mainly derived from the 3*d* electronic states, while the A-site ions form the frame of the crystal and also serve as a source of carriers. Perovskites are layered crystals and there are thus two possible surface terminations: the AO plane and the BO_2 plane.

Thin film synthesis of oxides is indispensable for fabricating actual electronic devices. Molecular layer deposition techniques of complex oxides have advanced rapidly since the discovery of high-T_c superconductors. Nowadays, the fabrication of artificial superlattices with atomic layer accuracy is possible[iii].

Investigation of the properties of heterointerfaces is necessary before new materials can be integrated into functional devices because in many devices the electronically active region is restricted to a thin layer at an interface. This is particularly true for

transistors. The performance of such devices is therefore dependent on accurate control of electronic states of thin interface layers. The current trend of continued downsizing of electronic components has meant that the characteristic dimensions of individual transistors have reached the nanometer scale[iv]. Critical lengths for device performance, such as sharpness of an interface, surface depletion layer thickness, and carrier mean-free-path are also on the nanometer scale. Designing and characterizing of ultra-thin films or nanostructures is a useful strategy for gaining an understanding of how to control the electronic states at heterointerfaces.

Moreover, ultra-thin oxide films that are only a few nanometers thick have found broad use in miniature electronic devices. Therefore it is obvious that improving the control over the crystal structure, electronic structure, and composition of oxide surfaces and interfaces is gaining importance in the design and development of new electronic devices. Above all, conductive nanowires are becoming unique and promising materials due to their strong anisotropy in electron confinement and conductivity. Nanowires can be used as interconnects or as building blocks for active switching or sensing devices.

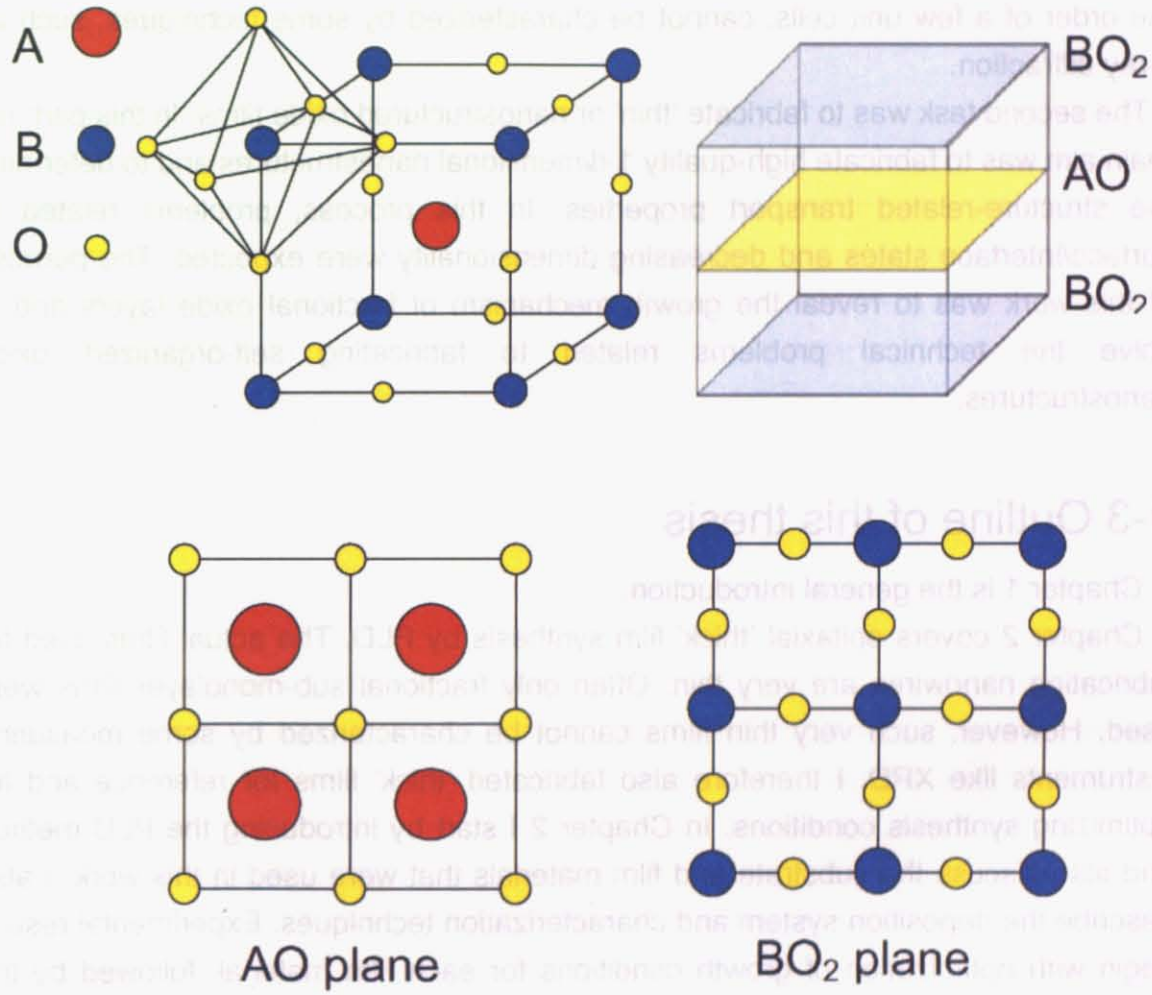

Fig.1-1
ABO_3 perovskite structure and the two possible surface terminations of a (001)-oriented lattice

1-2 Purpose of this study

The ultimate goal of this study is to fabricate conducting transition metal oxide nanowires. In order to achieve this goal, the work was divided into two sections. [

The first task was to fabricate 'thick' metal oxide films by Pulsed Laser Deposition (PLD) and to characterize them. Thick film were needed because very thin films, on the order of a few unit cells, cannot be characterized by some techniques, such as x-ray diffraction.

The second task was to fabricate 'thin' or nanostructured oxide films. In this part, my main aim was to fabricate high-quality 1-dimensional nanostructures and to determine the structure-related transport properties. In this process, problems related to surface/interface states and decreasing dimensionality were expected. The purpose of this work was to reveal the growth mechanism of fractional oxide layers and to solve the technical problems related to fabricating self-organized oxide nanostructures.

1-3 Outline of this thesis

Chapter 1 is the general introduction.

Chapter 2 covers epitaxial 'thick' film synthesis by PLD. The actual films used for fabricating nanowires are very thin. Often only fractional sub-monolayer films were used. However, such very thin films cannot be characterized by some measuring instruments like XRD. I therefore also fabricated 'thick' films for reference and for optimizing synthesis conditions. In Chapter 2 I start by introducing the PLD method and also discuss the substrate and film materials that were used in this work. I also describe the deposition system and characterization techniques. Experimental results begin with optimization of growth conditions for each film material, followed by the fabrication and characterization of the films.

Chapter 3 is about the fabrication of conducting perovskite oxide nanowires. At first, I refer to fabrication methods of nanowires and also review some relevant experimental results obtained from nanowires. This discussion points out some problems related to oxide nanostructures. Some improvements and solutions to known problems are shown in this Chapter, together with a detailed description of the fabrication and characterization of nanowire samples.

References

[i] J. G. Bednorz et al., Z. Phys. **B64**, 189 (1986)
[ii] Y. Tokura et al., Phys. Rev. B, **53**, R1689 (1996)
[iii] H. Koinuma et al., Solid State Commun., **80**, 9 (1991)
[iv] M. Saitoh et al., Appl. Phys. Lett. **79**, 2025 (2001)

Chapter 2
Fabrication of Thick Epitaxial Metal Oxide Film

2-1 Introduction

In principle, properties of thin oxide films, like transport, superconductivity, ferroelectricity, etc. should not depend on the film thickness if it remains larger than a few unit cells. In practice, however, large changes are observed even for relatively thick film layers. For example, in Mn-based perovskite oxides, there are several reports about thickness effects on transport and magnetic properties[i,ii,iii]. In many cases the resistivity becomes larger and ferromagnetism and magnetoresistance effects disappear as film thickness is reduced to a few nanometers. This is usually explained by the formation of a magnetic or an electrical 'dead layer' that represents a chemically or structurally altered layer close to the surface or the film-substrate interface.

The thickness of our target nanowire film is only one unit cell of the basic perovskite structure, which is typically around 4 Å. It is clear that at such layer thicknesses size effects are important. The characterization of such layers also becomes more difficult, because many techniques, like XRD, cannot observe a single unit cell layer, and other methods, like transport measurements, can alter the film properties due to surface contamination or damage. As a first step, therefore, I fabricated relatively thick films for reference and for optimizing synthesis conditions.

References

[i] J. Z. Sun et al., Appl. Phys. Lett., **74**, 3017 (1999)
[ii] M. Ziese et al., J. Appl. Phys., **91**, 9930 (2002)
[iii] R. B. Praus et al., Appl. Surf. Sci., **138-139**, 40 (1999)

2-2 Substrates and materials

In this study, $LaTiO_x$ (LTO) was used as a conducting material in nanowire structures. It is well known that the physical properties of $LaTiO_x$ ($3<x<3.5$) are very sensitive to the exact oxygen content[i]. Stoichiometric $LaTiO_3$ is an antiferromagnetic Mott-Hubbard type insulator with a charge gap of 0.2 eV. It has a distorted orthorhombic perovskite crystal structure ($GdFeO_3$ structure). Slight hole doping by introducing extra oxygen causes an immediate disappearance of the Mott gap and results in metallic conductivity. For $x>3.2$ the additional oxygen atoms order in infinite (110) perovskite planes and form a semiconducting layered structure for $x=3.4$. The $LaTiO_{3.5}$ ($La_2Ti_2O_7$) compound, also called the "2-2-7" phase, has a monoclinic structure and a robust ferroelectric phase. Especially in thin film studies, stoichiometric $LaTiO_3$ is difficult to grow because an extremely reducing atmosphere is needed. During the initial growth stage, the first few monolayers of $LaTiO_3$ can be formed due to a stabilizing effect of epitaxial lattice strain from the $SrTiO_3$ substrate. In thicker layers, however, the $La_2Ti_2O_7$ phase starts to form[ii]. According to published reports, conducting LTO films, mainly dominated by the $LaTiO_3$ phase, with a carrier concentration of $\sim10^{23}$ cm^{-3} can be grown at a relatively low oxygen pressure of $\sim10^{-6}$ Torr[iii]. Hole doping can also be achieved by substitution of La by Sr[iv]. In $LaTiO_3/SrTiO_3$ superlattices, doped carriers extend beyond the physical limits of the $LaTiO_3$ layer due to charge transfer between neighboring atomic layers, resulting in metallic conduction[v].

$SrTiO_3$ (STO) was used as a substrate material. As received, wet-etched $SrTiO_3$ substrates were used for depositing thick LTO films. A pre-annealing treatment was performed for substrates that were used for growing films thinner than 5 nm. The annealing was done at 1050 °C for 1 hour at an oxygen pressure of 10^{-6} Torr. STO is a band insulator[vi] with a band gap of ~3.2 eV. It can be readily doped to give an n-type semiconductor by substitution of Sr with La, or by introducing oxygen vacancies. Metallic conductivity is achieved when the carrier concentration exceeds 10^{18} cm^{-3} [vii]. Hall mobility increases with reducing temperature and can reach more than 10000 cm^2/Vs at low temperature[viii]. The residual resistance ratio (R.R.R.) is relatively high (>100)[ix]. Superconductivity appears in the 10^{19} to 10^{20} cm^{-3} carrier concentration range[x].

SrO was used for changing the termination layer of the $SrTiO_3$ substrates. $SrTiO_3$ can have two possible surface terminations, either the SrO plane or the

TiO_2 plane. As received, wet-etched $SrTiO_3$ substrates have a TiO_2 terminated surface. Single monolayer SrO films were used to convert the usual $SrTiO_3$ substrate terminating layer from TiO_2 to SrO.

Compound	a(Å)	b(Å)	c(Å)	Crystal structure
$LaTiO_3$	5.620 S(+1.77%)	5.604 S(+1.47%)	7.911 S(+1.29%)	Orthorhombic
$La_2Ti_2O_7$	13.02	5.546	7.817	monoclinic
SrO	5.160	-	-	cubic
$SrTiO_3$	3.905	-	-	cubic

Fig.2-2
Table of conducting material and substrates
S: mismatch to STO substrate

References

[i] F. Lichtenberg et al., Z. Phys. B, **82**, 211 (1991)
[ii] A. Ohtomo et al., Appl. Phys. Lett., **80**, 3922 (2002)
[iii] A. Schmehl et al., Appl. Phys. Lett., **82**, 3077 (2003)
[iv] Y. Tokura et al., Phys. Rev. Lett., **70**, 2126 (1993)
[v] A. Ohtomo et al., Nature, **419**, 378 (2002)
[vi] L. Pellegrino et al., Appl. Phys. Lett., **81**, 3849 (2002)
[vii] O. N. Tufte et al., Phys. Rev., **155**, 796 (1967)
[viii] H. P. R. Frederikse et al., Phys. Rev., **161**, 822(1967)
[ix] K. A. Müller et al., Phys. Rev. B, **19**, 3593 (1979)
[x] J. F. Schooley et al., Phys. Rev. Lett., **14**, 305 (1965)

2-3 Deposition system and characterization of films

2-3-1 Pulsed laser deposition

Pulsed laser deposition (PLD) is one of the physical vapor deposition (PVD) techniques, where target material is evaporated and the gas-phase precursors condense on a sample surface. In PLD, a high-power ultraviolet pulsed laser is fired on a target surface inside a vacuum chamber. The very high energy density at the target surface results in the ablation of a small amount of material from the target surface. The resulting atoms, molecules, ions or clusters are deposited on the substrate[i]. This technique is particularly suitable for oxide film synthesis because generally the melting point of oxides is quite high and it is therefore difficult to evaporate oxides by other means. A high-energy laser pulse, however, can evaporate any material. Another strong point of PLD is that chamber contamination is relatively low because the energy required to vaporize the solid target material is introduced optically from outside of the deposition chamber. In addition, the technique is not dependent on high vacuum, as required for example by molecular beam epitaxy. Due to this, oxygen can be fed into the reaction chamber at pressures of up to several hundred milli-torr, allowing relatively straightforward control of oxygen content in the film. The compositional deviation between the target and the films is small, because the ablation process is not element-selective. In most cases stoichiometry deviations can be ignored.

The biggest weakness of PLD is the difficulty of fabricating homogeneous films over a wide area. The chemical and structural homogeneity of films depends on the ablation plume radius, which in a typical system is limited to less than 1~2cm.

Molecular beam epitaxy (MBE) is a deposition method where source materials are thermally evaporated in high vacuum, under conditions where the mean free path of the vaporized particles is larger than substrate-target distance[ii]. The main advantage of MBE is that atomic layer level control of film thickness is possible over a wider area. When combined with RHEED, in situ monitoring of crystal growth during the deposition is possible and very high-quality films can be formed with low impurity concentrations. The drawback of MBE is the need for a separate evaporation source for each element.

Laser MBE combines the best features of PLD and MBE. A diagram of a laser MBE system is shown in Fig.2-3-1-1. This system is composed of an ultra-high vacuum deposition chamber, a KrF excimer laser for target evaporation, a RHEED monitoring system, and infrared laser heating for the control of the sample temperature.

The deposition chamber (Fig.2-3-1-2) is pumped by a turbo molecular pump (TMP) to achieve a base pressure of about $3x10^{-9}$ Torr. For ablation of targets, a KrF excimer laser (λ: 248nm, ThinFilmStar, TuiLaser (Fig.2-3-1-3)) is used. A pulsed laser beam with a width of about 20 ns is introduced in the chamber through a synthetic quartz window and focused onto the target surface. Up to six targets can be placed in the chamber. Targets can be easily exchanged without breaking vacuum by using a load lock chamber. In order to avoid fast erosion of the target surface, the targets are continuously scanned by computer-controlled stepping motors so as to ablate evenly the whole surface of the target.

The substrate is clamped on a sample holder made of stainless steel. Platinum paste is applied between a substrate crystal and a Ni susceptor, which is a part of the sample holder. The nickel insert is oxidized and absorbs infrared light from a heating laser. The nickel block effectively diminishes temperature variation over the sample surface and the platinum paste improves the thermal contact between the substrate crystal and the nickel block. The parts of the heat absorber that are not open to the heating laser and not in contact with the sample crystal, were covered with a Pt sheet, which functioned as a heat reflector, significantly improving the heating efficiency of the system. The substrate holder is shown in Fig.2-3-1-4.

The substrate-target distance can be chosen according to experimental needs. In most experiments, a distance of about 54 mm was used. The chamber also had a set of masks that could be inserted in front of the sample crystal in order to limit the film growth to a specific region on the substrate surface. The masks are mounted on computer-controlled linear drives. In this work, the masking system was used to grow samples with linear film thickness gradients. Process gas (oxygen) was introduced into the system through a stainless nozzle that pointed at the substrate, increasing the effective oxygen pressure in the vicinity of the substrate. A diode laser (λ: 976nm, JOLD-140-CAXF-6A JENOPTIK (Fig.2-3-1-5)) was used for substrate heating. The substrate temperature was monitored with an optical pyrometer.

The advantage of using a laser for sample heating is the high maximum

temperature that can be reached (maximum: 1300°C) and rapid heating/cooling, which is possible due to the low heat capacitance of the sample holder. Laser heating also helps to maintain a clean chamber and a low background pressure because the heat source is outside of the chamber, so miniaturization of the chamber is possible and homogeneous heating is achieved.

Scanning RHEED was used in this system for in situ monitoring of growth dynamics and atomic level growth control. A narrow electron beam emitted from the RHEED gun is scattered from the sample surface and forms a diffraction pattern on a phosphor screen. The image is captured with a video camera and analyzed in real time on an attached computer. A special feature of this RHEED system is the ability to scan the electron beam across the sample surface under computer control. The RHEED gun was differentially pumped, and could be used at oxygen pressures of up to 1 mTorr.

All aspects of the deposition process, including the sample temperature, the KrF excimer laser triggering, moving of the masks, selecting and scanning the targets, RHEED electron beam position, and gas pressure were controlled by LabVIEW (National Instruments). An image of the control panel is shown in Fig.2-3-1-6.

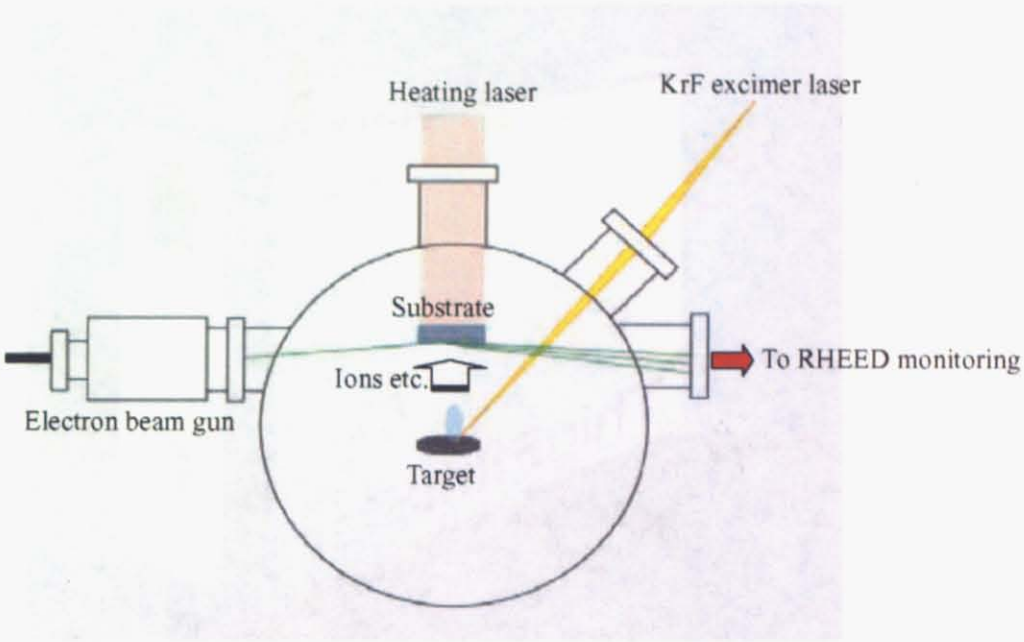

Fig.2-3-1-1 Laser MBE system

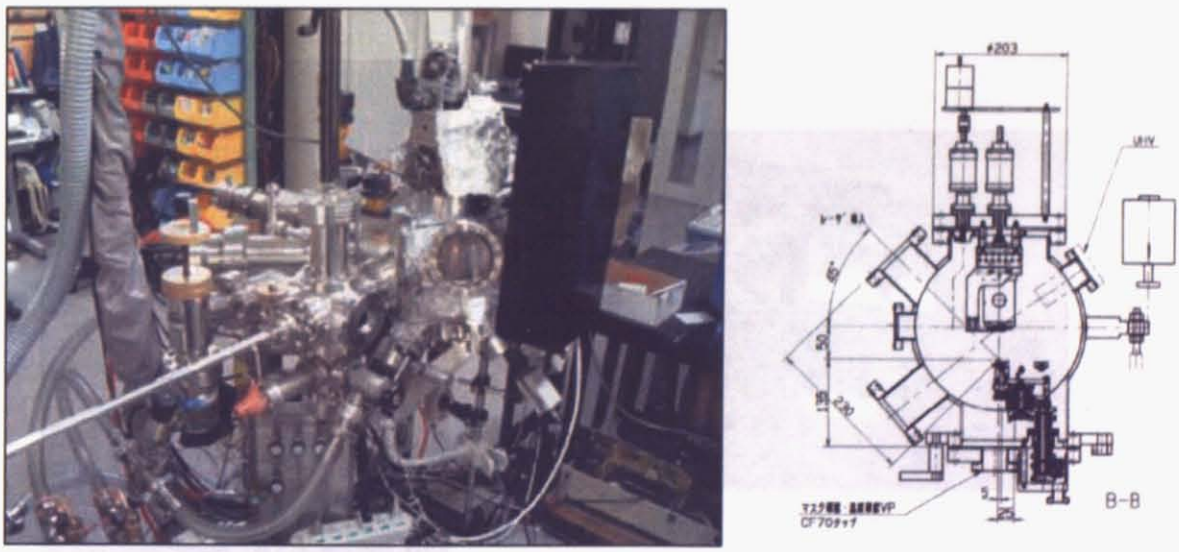

Fig.2-3-1-2 Deposition chamber

Fig.2-3-1-3 Excimer laser

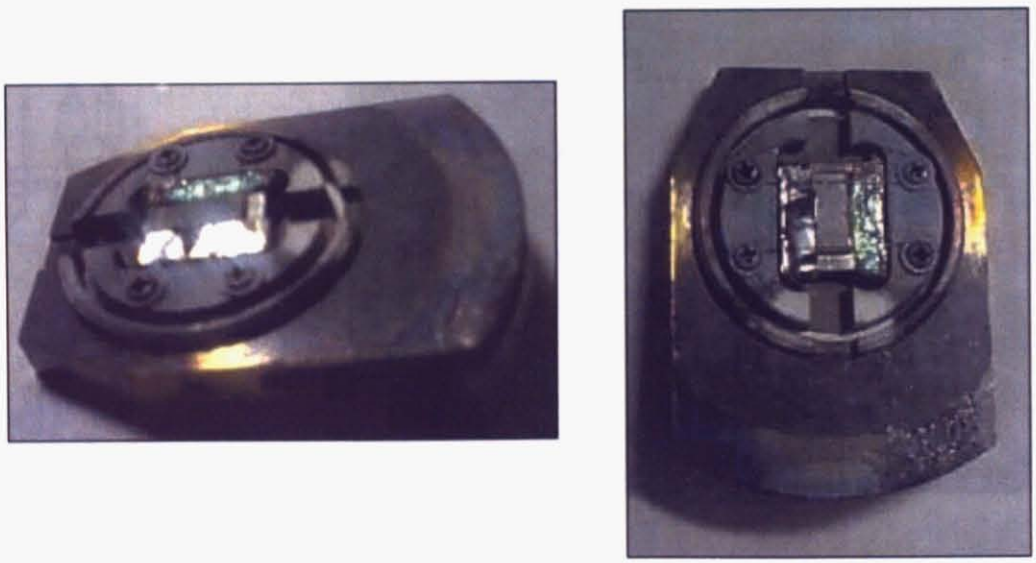

Fig.2-3-1-4 sample holder

Fig.2-3-1-5 Heating laser

Fig.2-3-1-6 Display image of the LabVIEW control program

2-3-2 Reflection High Energy Electron Diffraction

Reflection high energy electron diffraction (RHEED) is a powerful technique for studying surface structures of reasonably flat surfaces[iii] as well as surface phase transitions. RHEED is sensitive to structural changes on crystal surfaces that may occur as a result of heat treatment or that accompany crystal growth. Therefore, RHEED is widely used as an in-situ probe to monitor the growth rate and surface morphology evolution of thin film surfaces both for research purposes and in industry.

The geometry of RHEED is quite simple (Fig.2-3-2-1). An accelerated electron beam (5 – 100 keV) is incident on the surface with a glancing angle (≈3 °) and is reflected. The high energy of the electrons would result in high penetration depth. However, because of the glancing angle of incidence, only a few topmost atomic layers are probed. This is the reason for the high surface sensitivity of RHEED. While interacting with the surface, electrons may reflect, forming the specular beam, or diffract, forming a diffraction pattern that depends on the atomic structure of the surface layer.

Conceptually, perfectly flat surfaces should result in a diffraction pattern that consists of spots arranged on Laue rings. However, because of the non-idealities in the electron beam and the sample's surface, streaks appear instead of spots. Transmission spots are sometimes observed on relatively rough surface generated by island growth.

The specular reflection intensity is proportional to the surface roughness, so observation of this parameter during deposition gives real-time information about film growth dynamics. By analyzing the specular intensity behavior, it is possible to decide whether the growth is 2 or 3-dimensional and whether the growth proceeds in a layer-by-layer or step-flow mode. Layer-by-layer growth is useful for producing two-dimensional, layered structures. A crystal growth model and the corresponding behavior of the specular spot intensity are shown in Fig.2-3-2-2. Step-flow growth occurring at higher temperature shows also characteristic specular spot intensity behavior (discussed in chapter 3).

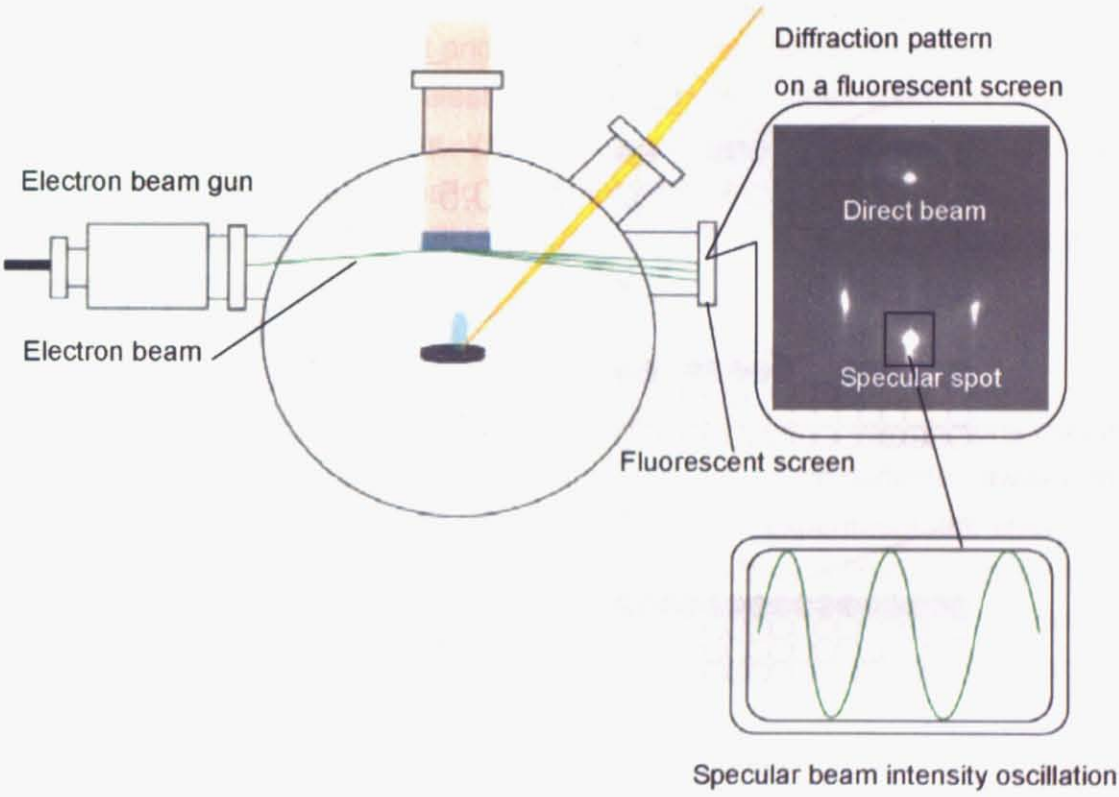

Fig.2-3-2-1 RHEED system

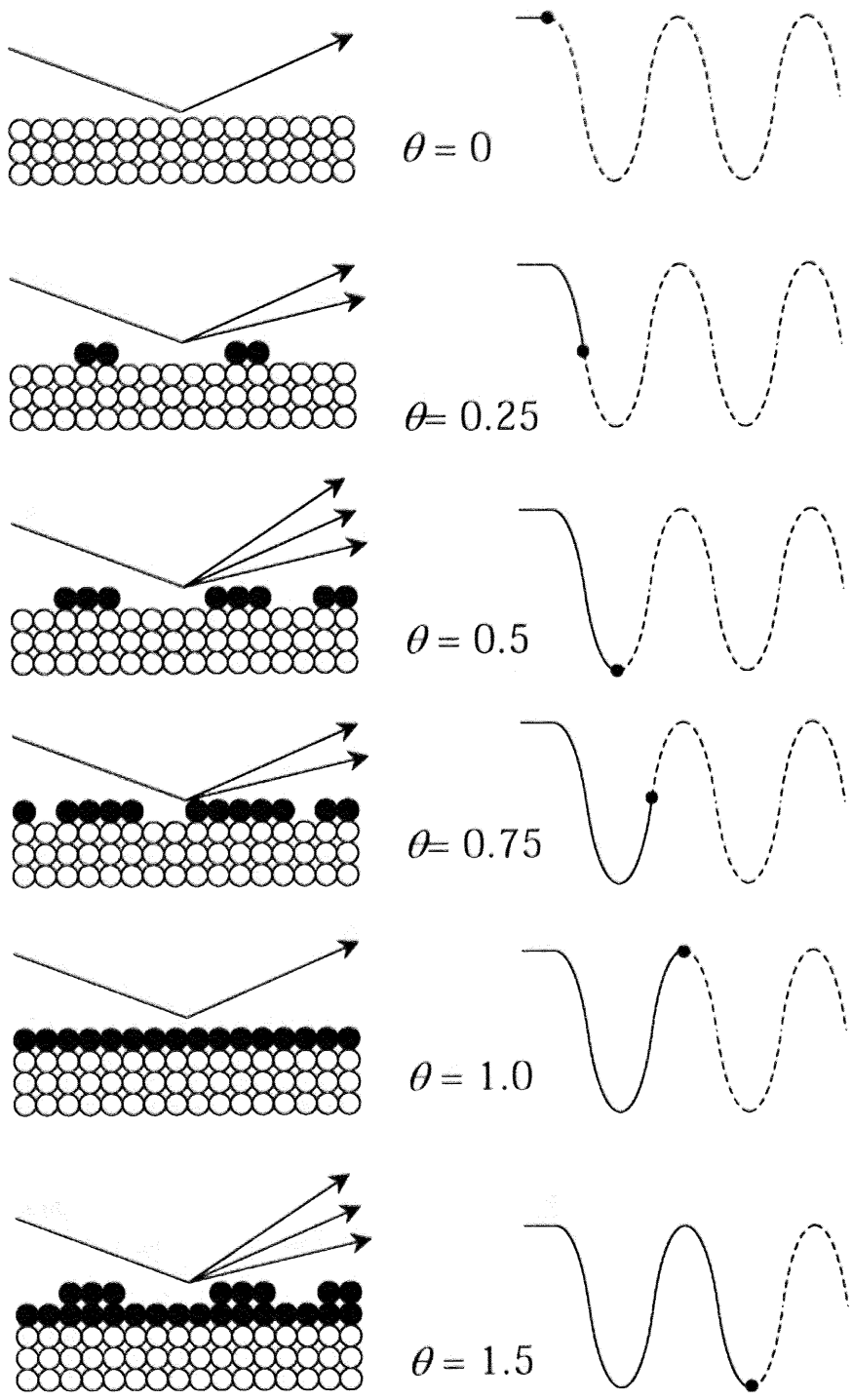

Fig.2-3-2-2
Layer-by-layer growth and RHEED specular intensity oscillation

2-3-3 X-ray diffraction

X-ray diffraction (XRD) is a useful tool for studying crystal structures. In case of thin films, XRD is often used to determine crystal orientation and crystallinity of epitaxial films.

X-ray Generation & Properties

X-rays for diffraction experiments are produced by either x-ray tubes or synchrotron radiation. In an x-ray tube, x-rays are generated when a focused high-energy electron beam hits a stationary or rotating solid target. As electrons collide with atoms in the target and slow down, a continuous spectrum of x-rays are emitted. The high-energy electrons also eject inner shell electrons in atoms through the ionization process. When a free electron fills the shell, an x-ray photon with energy characteristic of the target material is emitted. A Cu x-ray source was used in this work. The Cu target emits 8 keV x-rays with a wavelength of 1.54 Å.

Lattice Planes and Bragg's Law

X-rays primarily interact with electrons in atoms. When x-ray photons collide with electrons, some photons from the incident beam will be deflected away from the direction where they original travel. In a diffraction experiment, the energy of the scattered x-rays does not change. The scattered, or diffracted waves from different atoms can interfere with each other and the resultant intensity distribution can be used to analyze the lattice parameters and atomic positions in the sample crystal.

The diffraction angle of the diffraction peaks is directly related to the atomic distances. The out-of-plane lattice parameter of a film is determined from a $\theta/2\theta$ scan according to Bragg's law,

$$2d \sin\theta = n\lambda,$$

where λ is the x-ray wavelength, n is an integer, and θ is the diffraction angle (Fig.2-3-3-1).

Powder Diffraction

Powder XRD (X-ray Diffraction) is the most common technique for characterizing materials. In this case a powder sample is used and a conventional theta/2 theta scan is used to measure the lattice spacings present

in the crystals. The technique can also be used for studying polycrystalline solids and thin films, although only a subset of diffraction peaks is typically observed, depending on the orientation of the sample crystal in the diffractometer. In this work, conventional powder diffraction techniques were used to measure the out-of-plane lattice parameters of the thin film samples.

Thin Film Diffraction

Although a conventional powder diffractometer can be used for analyzing the out-of-plane lattice parameters of thin films as well, there are also dedicated diffraction machines designed to characterize thin films. The techniques used in this work, for example, included the measurement of rocking curves, where only the theta angle of the sample is changed. This measurement mode can be used to analyze the crystallinity of a sample. Better crystallinity would result in a narrower rocking curve width.

A photograph and schematic view of the instrument are shown in Fig.2-3-3-2.

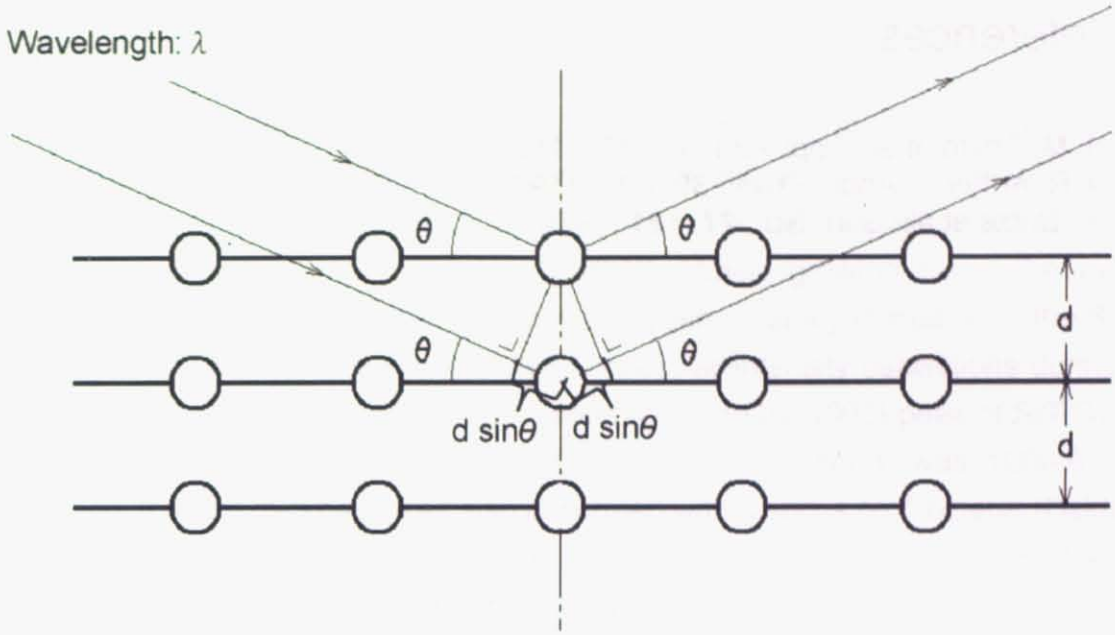

Fig.2-3-3-1 Principle of XRD

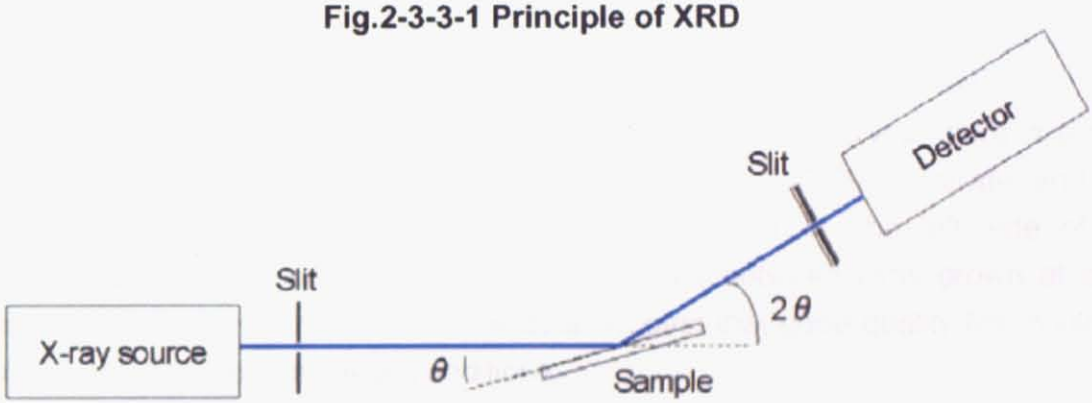

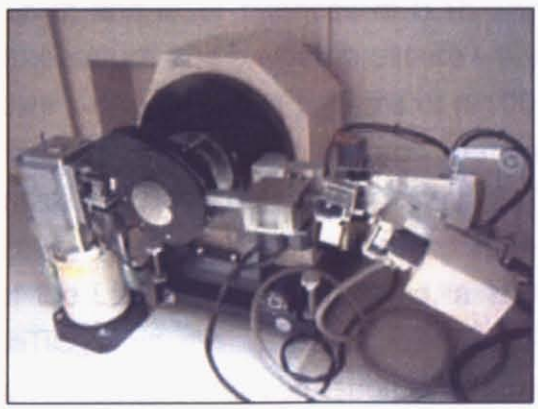

Fig.2-3-3-2 X-ray diffractometer

References

[i] H. M. Smith et al., Appl. Opt., **4**, 147 (1965)
[ii] J. R. Arther, J. Appl.. Phys., **39**, 4032 (1968)
[iii] K. Britze et al., Surf. Sci., **77**, 131 (1978)

2-4 Optimization of growth conditions for fabricating thick films

The growth conditions of $SrTiO_3$ films were optimized first so as to obtain good crystallinity. As the first step in the optimization process, a single crystal $SrTiO_3$ target was ablated at a laser fluence of 0.25 J/cm^2 and at a laser repetition rate of 2Hz or 5Hz. The substrate temperature was 700 °C. When growing films, the oxygen pressure was fixed at $1x10^{-6}$ Torr to prevent oxygen vacancy formation in the $SrTiO_3$ substrate. Fig.2-4-1 (a) shows the RHEED specular intensity oscillations during film growth and the x-ray diffraction patterns taken close to the (002) peak of $SrTiO_3$. The film thickness, calculated from the RHEED oscillation period, was 1000 Å. After deposition, the film thickness was also confirmed with a stylus profilometer (Dektak).

As shown in Fig.2-4-1 (a)-1 and -2, the specular RHEED intensity oscillated without showing a decay in amplitude, which means that the growth proceeded in a layer-by-layer mode and it can therefore be assumed that one intensity oscillation period corresponds to a growth of a single unit cell layer of $SrTiO_3$. This type of RHEED behavior also implies epitaxial growth. The deposition speed estimated from the RHEED oscillation period was 0.13 Å/pulse. In the XRD curves, there is almost no difference between the diffraction patterns of the $SrTiO_3$ substrate and the homoepitaxial $SrTiO_3$ films except for a small shoulder on the left side of the substrate peak. There was no detectable difference between films grown at laser repetition rates of 2Hz and 5Hz. These data suggest that good quality film could be obtained under these fabrication conditions.

The next material to optimize was $LATiO_3$. The parameter that was optimized for was the conductivity of thick $LaTiO_3$ films. A sintered $La_2Ti_2O_7$ target was ablated at a laser repetition rate of 5Hz and laser fluences of 0.15 J/cm^2, 0.25 J/cm^2 and 0.51 J/cm^2. The substrate temperature and oxygen pressure were 700 °C and $1x10^{-6}$ Torr, respectively. Fig. ** shows x-ray diffraction patterns of a 1000 Å $LaTiO_3$ film grown at 700 °C on a $SrTiO_3$ substrate. During the initial growth stage, the $LaTiO_3$ phase can be stabilized by the epitaxial lattice strain effect of the $SrTiO_3$ substrate. In thicker layers, however, the $La_2Ti_2O_7$ phase easily starts to form[i]. Therefore in order to reduce the likelihood of the $La_2Ti_2O_7$ phase forming, a 100 Å $SrTiO_3$ capping layer was deposited on the $LaTiO_3$ films.

The XRD pattern showed a peak that corresponds to strained $LaTiO_3$. $LaTiO_3$ has an orthorhombic structure. Its lattice constants are a=5.620 Å, b=5.604 Å, c=7.911 Å. The lattice can also be viewed as a distorted perovskite structure, which is pseudo-cubic. If the lattice constants of orthorhombic structure are 'a', 'b' and 'c', the lattice constants of a pseudo-cubic unit cell can be calculated

as $\sqrt{a^2+b^2}/2$, $\sqrt{a^2+b^2}/2$, and $c/2$. (Fig.2-4-2 (a)).

As mentioned above, the $LaTiO_3$ phase is stabilized and distorted by the effect of epitaxial lattice strain from the $SrTiO_3$ substrate. Therefore, the lattice constant along the *c*-axis can be approximated by finding the volume of a $LaTiO_3$ pseudo-cubic cell and dividing it by the square of the 3.905 Å, which is the lattice constant of $SrTiO_3$. (Fig.2-4-2 (b)) The out-of-plane lattice spacing obtained in this way is 4.084 Å, which corresponds to a diffraction angle 2θ of 21.74° in. Strained $LaTiO_3$ is thus expected to show a peak at 21.74° where the dotted line is drawn in Fig.2-4-3 (a). The sample where the $LaTiO_3$ film peak was closest to the expected position of a fully strained pseudo-cubic lattice was grown at a laser fluence of 0.25 J/cm^2. The rocking curve of this sample is shown in Fig.2-4-3 (b). The rocking curve FWHM, which should be as small as possible in a good film, was 0.056° at a fluence of 0.15 J/cm^2, 0.052° at 0.25 J/cm^2, and 0.068° at 0.51 J/cm^2. Based on the film peak position in the θ-2θ scans and the rocking curve FWHM, it can be concluded that the laser fluence of 0.25 J/cm^2 is optimal.

The samples mentioned so far were measured in the as-grown state, without any post-processing. It is known that $SrTiO_3$ can easily lose oxygen and become conducting[ii]. To decrease this effect, post-annealing in a furnace was done to compensate the oxygen vacancies that may have formed in the $SrTiO_3$ substrate. The annealing conditions were: 400 °C, 6 hours, in air. After post-annealing, the film peak position in the θ-2θ scan and the rocking curve width changed as shown in Fig.2-4-4. The film peaks shifted to lower diffraction angles, which correspond to larger out-of-plane lattice constants. The rocking curves became broader. For the optimal sample grown at 0.25 J/cm^2, the FWHM increased from 0.052° to 0.152°. The rocking curve width of other samples couldn't be estimated because of the too broad shape line shapes. This means that the quality of the crystal was reduced by the annealing, probably due the formation of the $La_2Ti_2O_7$ phase.

Fig.2-4-5 shows how the fabrication temperature and laser pulse repetition rate affected the properties of the $LaTiO_3$ films. The dotted line corresponding to the expected position of fully strained $LaTiO_3$ is again shown at 21.74°. The laser repetition rate was either 5 Hz or 1 Hz. Growth temperatures were 700 °C and 1100 °C. The oxygen pressure was always fixed at 1×10^{-6} Torr. The film peak of a sample grown at 1100 °C was very broad and weak. On the other hand, at a growth temperature of 700 °C the film peak was considerably sharper and the peak position was closer to the lattice constant of $LaTiO_3$. This means that 700 °C is better for the growth of thick $LaTiO_3$ films.

The growth conditions of SrO films were optimized for better epitaxial growth on $SrTiO_3$. A sintered SrO_2 target was ablated at laser fluences of 0.25 J/cm^2 and 0.91 J/cm^2. The substrate temperature was either 550 °C or 700 °C. When growing the

films, the oxygen pressure was fixed at $1x10^{-6}$ Torr to prevent oxygen vacancy formation in the $SrTiO_3$ substrate. Fig.2-4-6 shows the XRD pattern of a 1000 Å SrO film grown on an $SrTiO_3$ substrate. All samples were covered with STO capping layer. STO capping layer was used in order to prevent surface oxidation and to hold the $LaTiO_{3+\delta}$ crystal structure.

In the XRD pattern of a sample grown at 0.25 J/cm^2 and 550 °C, no SrO film peak could be observed. An SrO film is supposed to show a peak at 34.73°. This value corresponds to the lattice constant of the SrO (002) plane, which has a lattice spacing of 2.581 Å. The SrO (002) peaks emerged in samples grown at higher laser fluence. At 0.91 J/cm^2, film peak were visible in samples grown both at 550 °C and 700 °C.

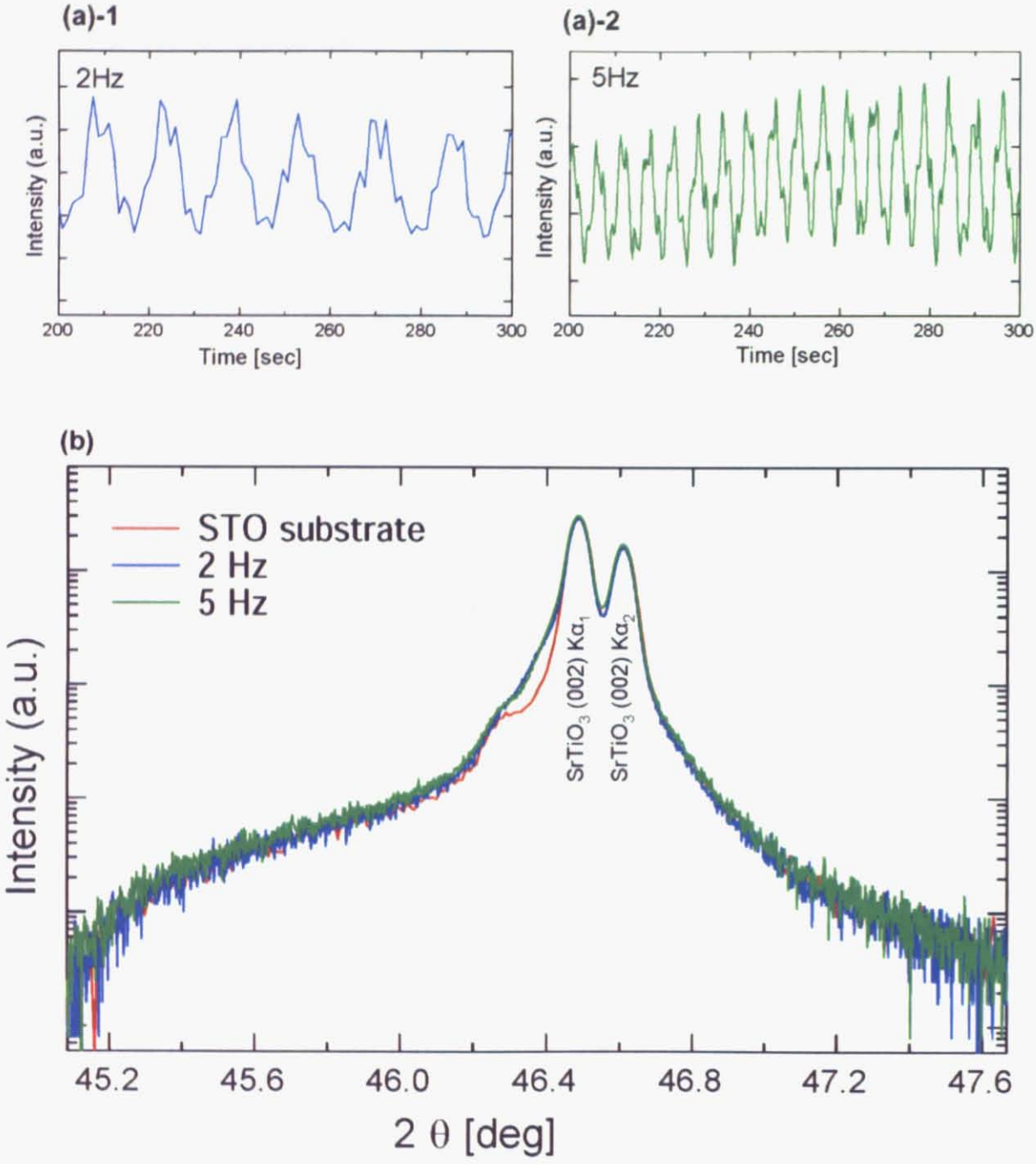

Fig.2-4-1

Laser repetition rate effect on $SrTiO_3$ homoepitaxial film grown at 700 °C

(a) RHEED intensity oscillation (b) XRD pattern

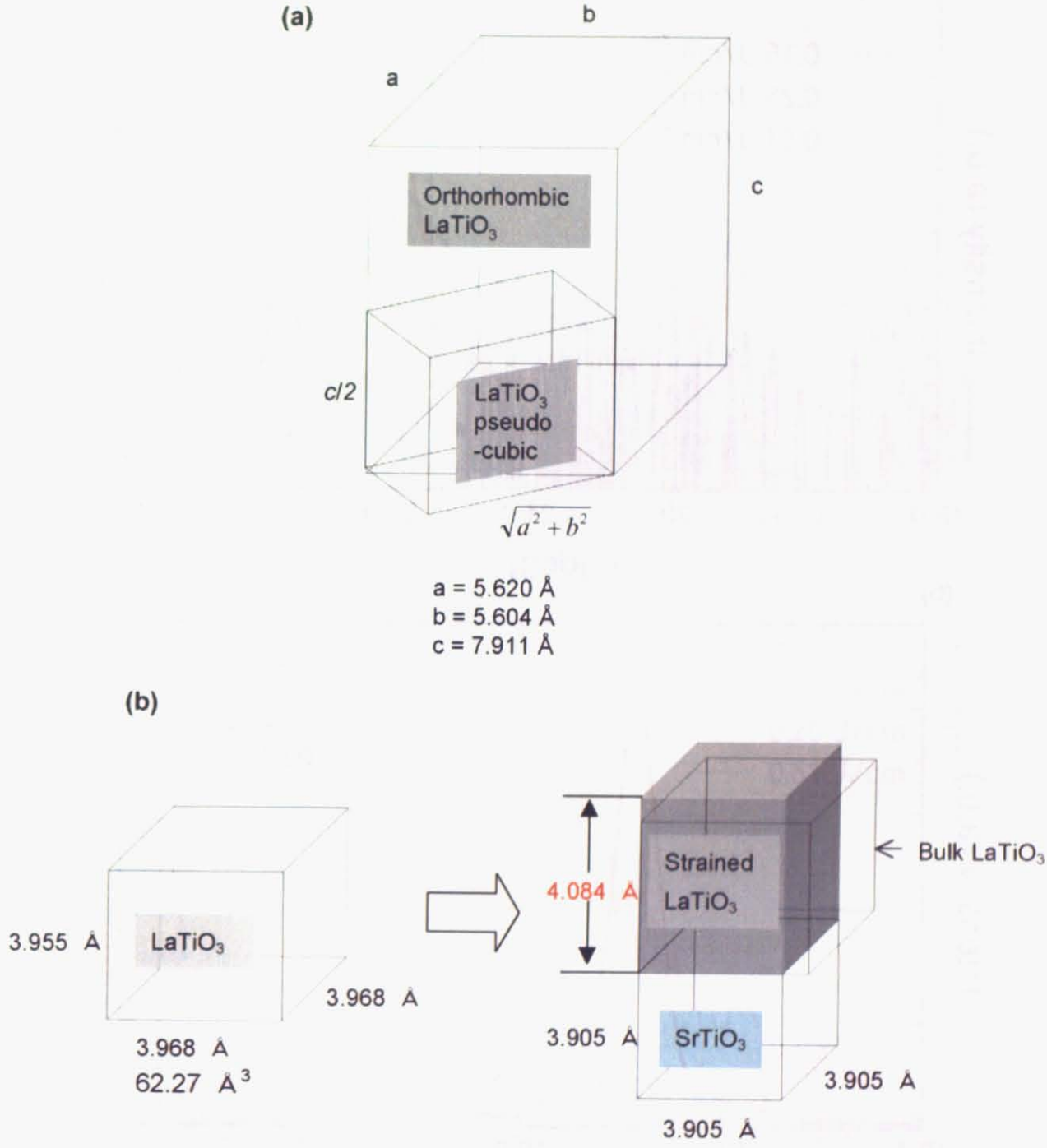

Fig.2-4-2

Schematic of (a) comparison of the orthorhombic and pseudo-cubic unit cells of $LaTiO_3$ and (b) strained $LaTiO_3$ film on a $SrTiO_3$ substrate

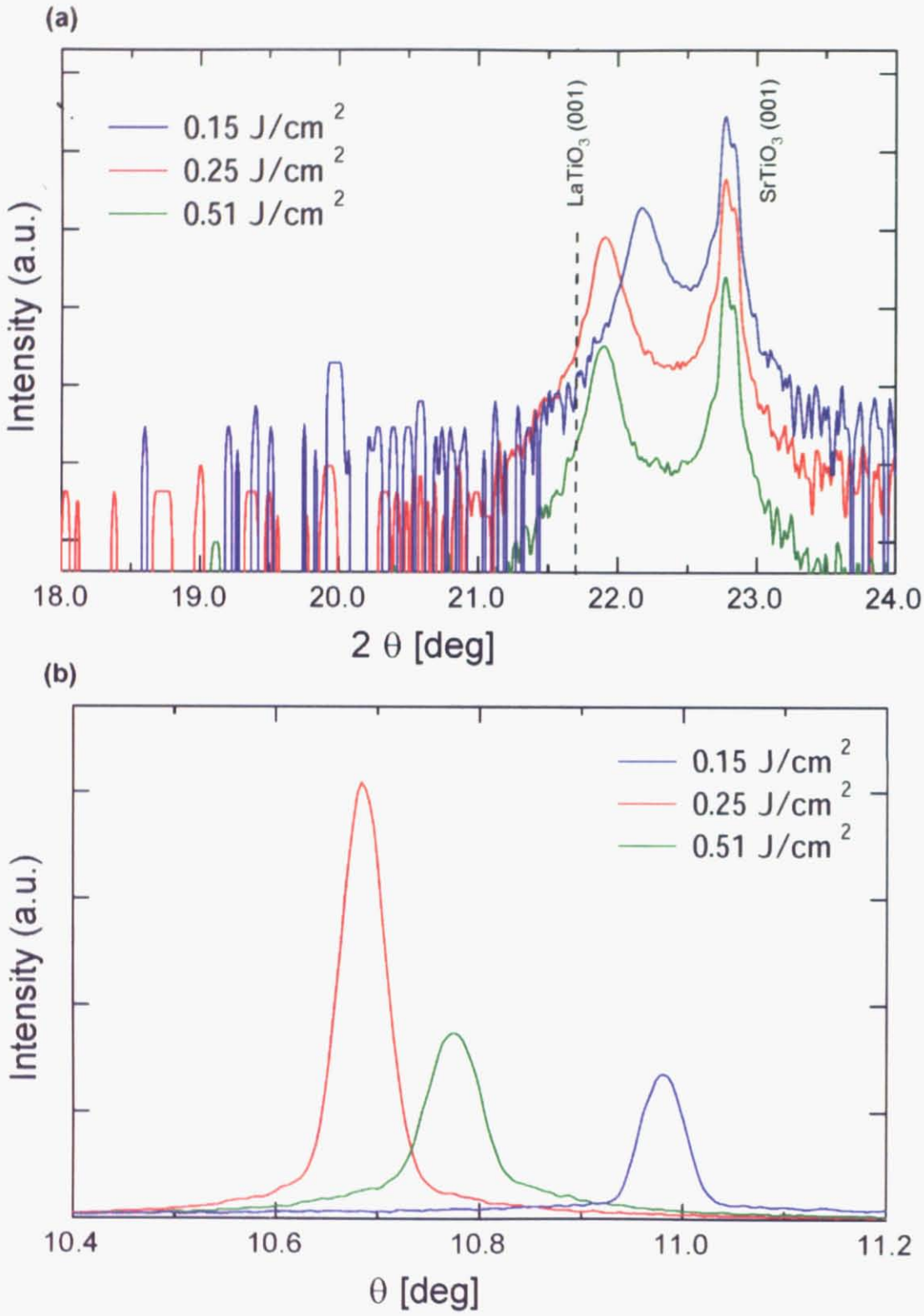

Fig.2-4-3

Laser fluence effect on as-grown $LaTiO_3$ films on $SrTiO_3$ substrates (a) XRD pattern (b) XRD rocking curve.

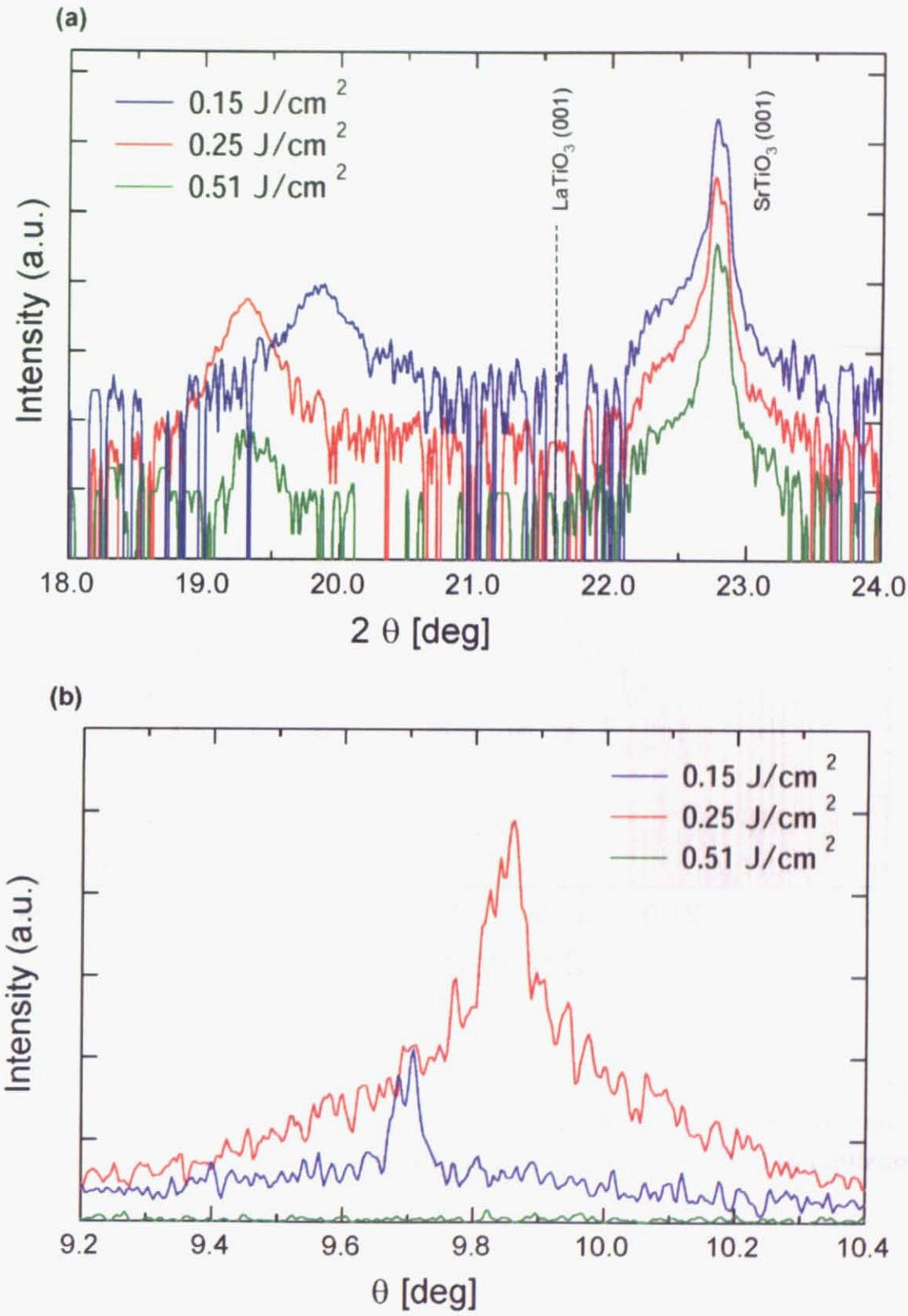

Fig.2-4-4

(a) XRD patterns and (b) XRD rocking curves of annealed $LaTiO_3$ films on $SrTiO_3$, grown at various laser fluences.

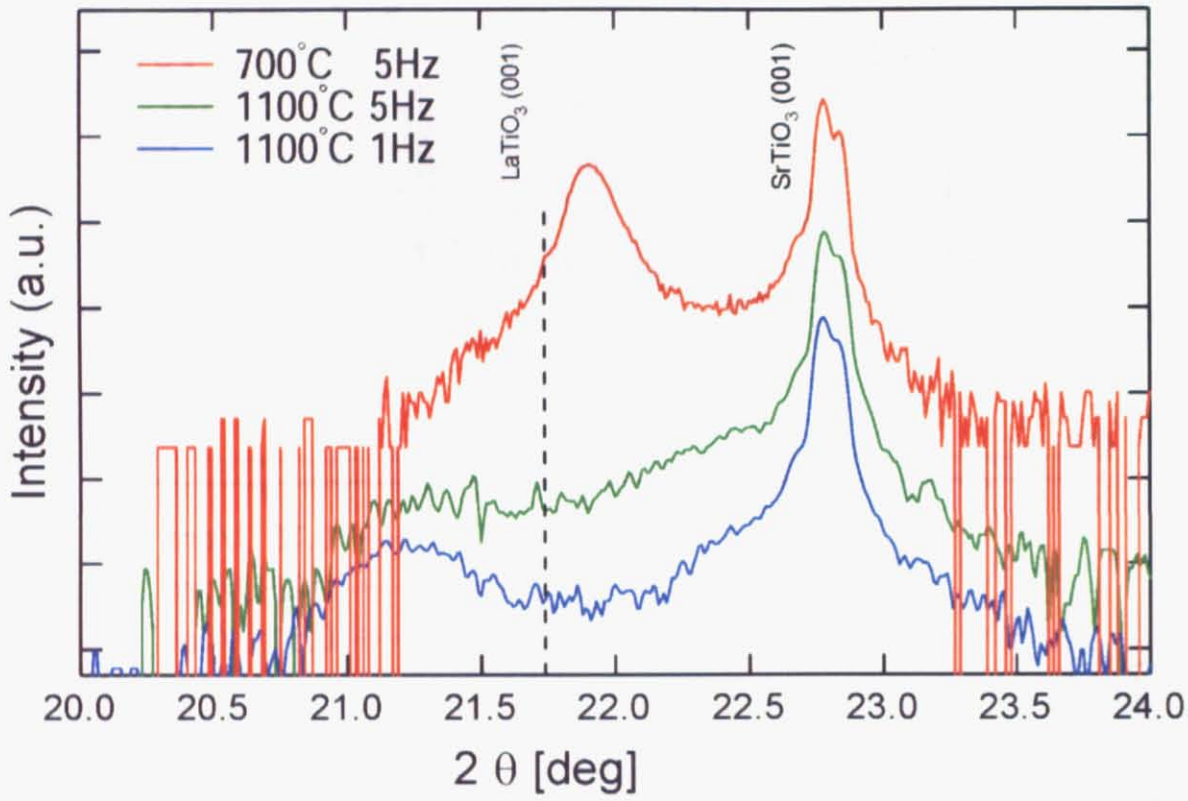

Fig.2-4-5

The effect of changing the laser repetition rate on the diffraction peak position of $LaTiO_3$ films on $SrTiO_3$ substrates.

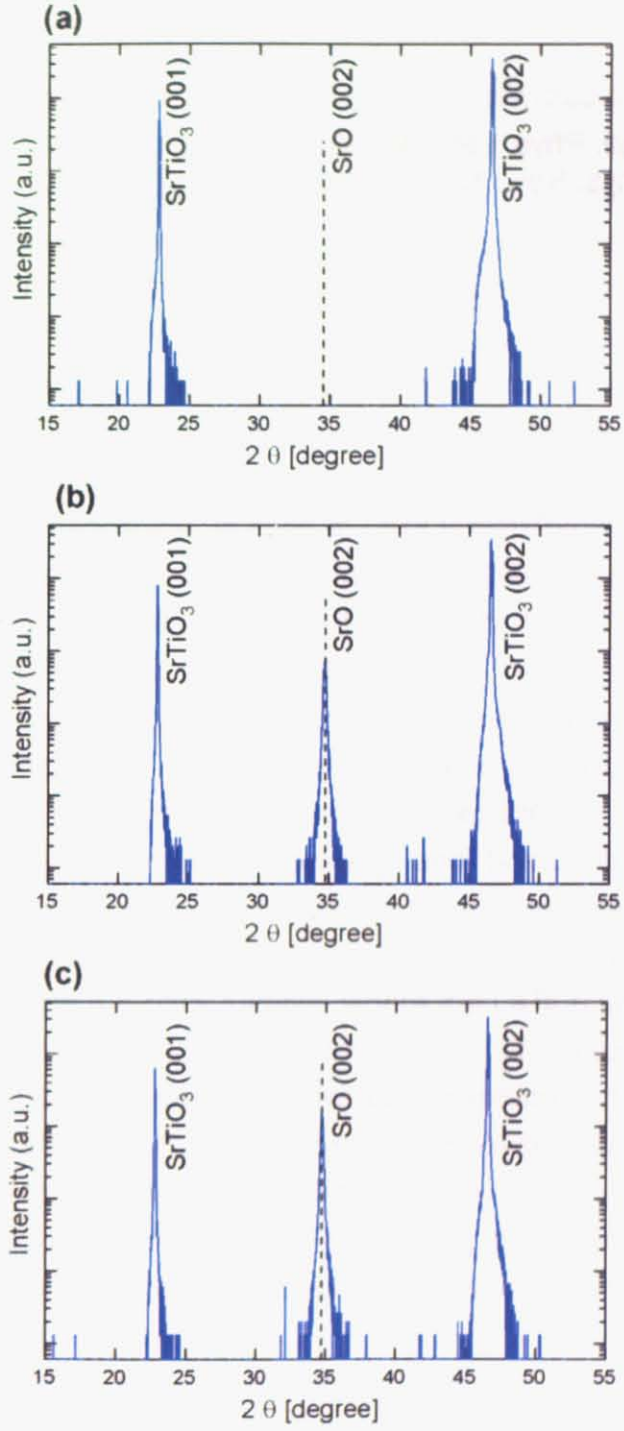

Fig.2-4-6

Comparison of diffraction patterns of SrO films grown on $SrTiO_3$ at (a) 550 °C, 0.25 J/cm^2, (b) 550 °C, 0.91 J/cm^2, and (c) 700 °C, 0.91 J/cm^2.

References

[i] A. Ohtomo et al., Appl. Phys. Lett., **80**, 3922 (2002)
[ii] O. N. Tufte et al., Phys. Rev., **155**, 796 (1967)

2-5 Thickness effect in $LaTiO_3$ films

The growth conditions for $LaTiO_3$ were originally optimized for relatively thick layers, where the film structure could be studied by x-ray diffraction. The ultimate goal, however, was to use single-unit cell films and even fractional layers for transport studies. Due to this, a series of samples was prepared with systematic thickness changes. All samples were grown under the optimal process conditions, at a substrate temperature of 700 °C and an oxygen pressure of 1×10^{-6} Torr. The excimer laser repetition rate was 5Hz and the fluence was set at 0.25 J/cm^2. All samples had a $SrTiO_3$ capping layer on the $LaTiO_3$ films. A series of AFM images (1 μm x 1 μm) of the samples are shown in Fig.2-5-1. The images were taken after $SrTiO_3$ capping layer deposition. In case of $LaTiO_3$ films grown on $SrTiO_3$ substrates, a step and terrace film surface was observed for film thicknesses of less than 150 Å.

The temperature dependence of sheet resistance for all $LaTiO_3$ films grown on $SrTiO_3$ is shown in Fig.2-5-2 (a). The data shown in Fig.2-5-2 (a) was measured immediately after deposition before any post-annealing treatments. All samples showed metallic conductivity. The smallest thickness that was mapped in this series of samples was 8 Å. An attempt was made to exclude the conductivity induced in $SrTiO_3$ by the high-temperature processing and bombardment of the substrate surface with high-energy ions in the deposition plume. Post-annealing was performed in an attempt to heal this type of damage in $SrTiO_3$. The data shown in Fig.2-5-2 (b) was measured from the 8 Å-thick sample, where the $LaTiO_3$ layer thickness was only 2 perovskite unit cells. Generally, electron doped STO (such as STO with large density of oxygen vacancy) with a carrier concentration in the range of 10^{18}~10^{19} shows a relatively large R.R.R., typically reaching several hundred[i], in part because of the very high electron mobility at low temperature in STO. The residual resistance ratio (R.R.R.) of the post-annealed 8 Å-thick sample reached about 20. While the as-grown 8 Å-thick sample reached about 1500. This suggests that post-annealing help to fill the oxygen vacancy.

A resistivity plot of the $LaTiO_3$ films is shown in Fig.2-5-2(c). As the thickness of the $LaTiO_3$ layer was reduced, the resistivity decreased. This behavior can be understood by assuming that in thicker films a gradual formation of the $La_2Ti_2O_7$ phase takes place. This phase is insulating, increasing the average resistivity of the films. The thicker films appear to have a larger proportion of the (227) phase, and the calculated resistivity is thus higher.

Figs. 2-5-3(a) and (b) show the XRD patterns for three thicker samples before and after the post-annealing treatment. The variation of the lattice parameters of the films is shown in Fig2-5-3(c). The dotted lines in the graphs show the point where the peak of distorted $LaTiO_3$ (001) pseudo-cubic peak was expected to be, assuming a lattice

constant of 4.084 Å. The film peaks in the as-grown samples are near the dotted line. On the other hand, after annealing the $LaTiO_3$ peaks shifted further away from the dotted line. This data suggest that the post annealing not only compensated the oxygen vacancies in $SrTiO_3$, but also changed the structure and phase of the $LaTiO_3$ films.

In order to use $LaTiO_x$ as material for nanowires, it is necessary to analyze which crystal phase forms during film growth. Since the perovskite $LaTiO_{3+\delta}$ phase is metallic and the $La_2Ti_2O_7$ phase is insulating, it is possible to determine which phase is in a thin film sample by measuring the optical absorption that is due to the presence of free carriers in a film. This technique can be used even for very thin film layers, where normal x-ray diffraction analysis would not be possible.

A Jasco V570 UV-VIS-NIR Spectrophotometer (Fig.2-5-4 (a)) was used to estimate the relative sheet resistances of various samples with different $LaTiO_x$ film thicknesses. During the initial growth stage, the first few monolayers of conducting $LaTiO_{3-\delta}$ can be formed due to a stabilizing effect of epitaxial lattice strain from the $SrTiO_3$ substrate. In thicker layers, however, the insulating $La_2Ti_2O_7$ phase starts to form[ii]. Since the metallic layer may only be a few unit cells-thick, it is difficult to confirm the presence of the $LaTiO_3$ phase by X-ray diffraction, which can only detect the signal of thick (>100Å) film. By using the UV-VIS-NIR spectrophotometer, the transmittance of wavelength dependence can be obtained. In this case, the absorption around 1800 nm, which corresponds to the density of the free carriers in the film, was measured. The instrument can be used to measure both the transmitted and reflected intensity of light, labeled It and Ir, respectively in Fig.2-5-4(b). The free carrier density can thus be estimated even in very thin layers. Fig. 2-5-4(c) shows the wavelength dependence of transmittance of $LaTiO_3$ films measured with the UV-VIS-NIR spectrophotometer. The thickness dependence of transmittance at 1800 nm is shown in Fig.2-5-5(a). Assuming that absorption occurs in the film, the transmittance should increase in thinner films. However this graph shows the reverse behavior. For comparison, the thickness dependence of room-temperature resistivity of annealed samples is shown in Fig.2-5-5 (b). The plots in Figs. 2-5-5(a) and (b) show similar tendencies. As the film thickness decreases, the resistivity should increase if the film consists of uniform material. This data shows that the $SrTiO_3$ substrate and the capping layer stabilize the $LaTiO_{3+\delta}$ phase and this effect is significant in the thinner films even after post-annealing. Due to this, thinner films have higher conductivity and larger free carrier density. It is thus reasonable to expect that $LaTiO_3$ can be used for fabricating metallic nanowires.

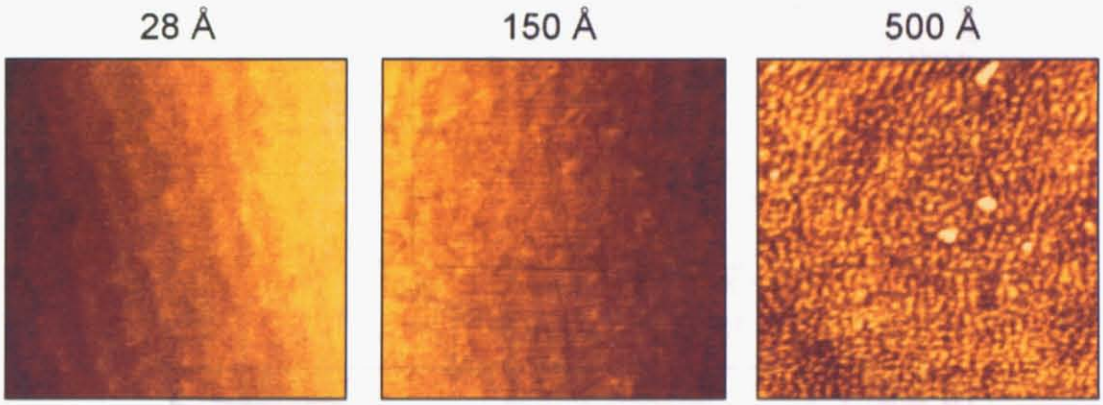

Fig.2-5-1
AFM images of $SrTiO_3$ capped $LaTiO_3$ films of variable thickness, grown on $SrTiO_3$ substrates.

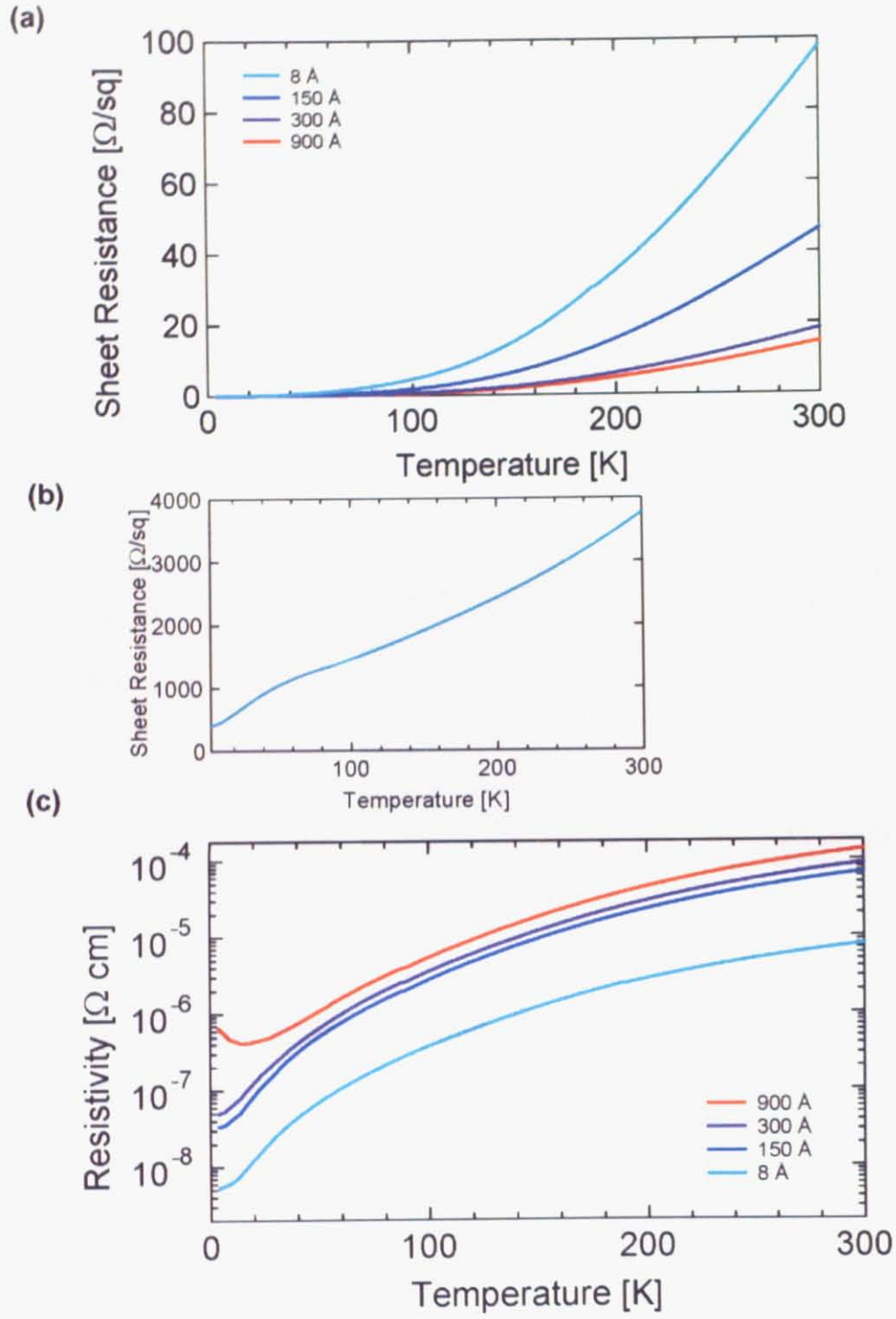

Fig.2-5-2

(a) Temperature dependence of sheet resistance of as-grown $LaTiO_3$ films on $SrTiO_3$ substrates.

(b) Temperature dependence of sheet resistance of an annealed 8 Å-thick $LaTiO_3$ film grown on a $SrTiO_3$ substrate.

(c) Temperature dependence of resistivity of $LaTiO_3$ films grown on $SrTiO_3$ substrates

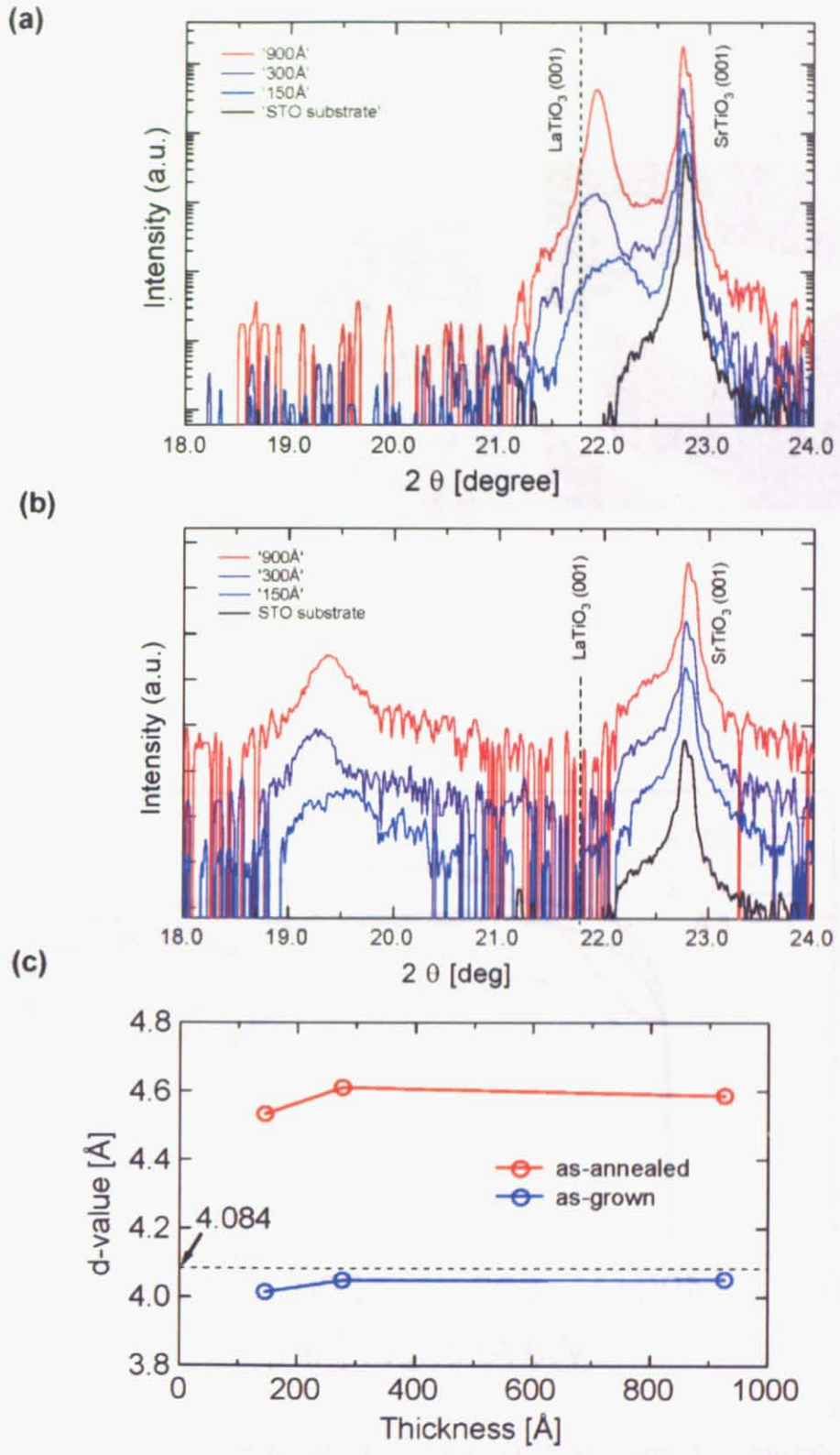

Fig.2-5-3

(a) XRD patterns of as-grown $LaTiO_3$ films with various thicknesses, grown on $SrTiO_3$. (b) XRD patterns of the same samples after post-annealing. (c) Thickness dependence of the lattice constants of $LaTiO_3$ films grown on $SrTiO_3$.

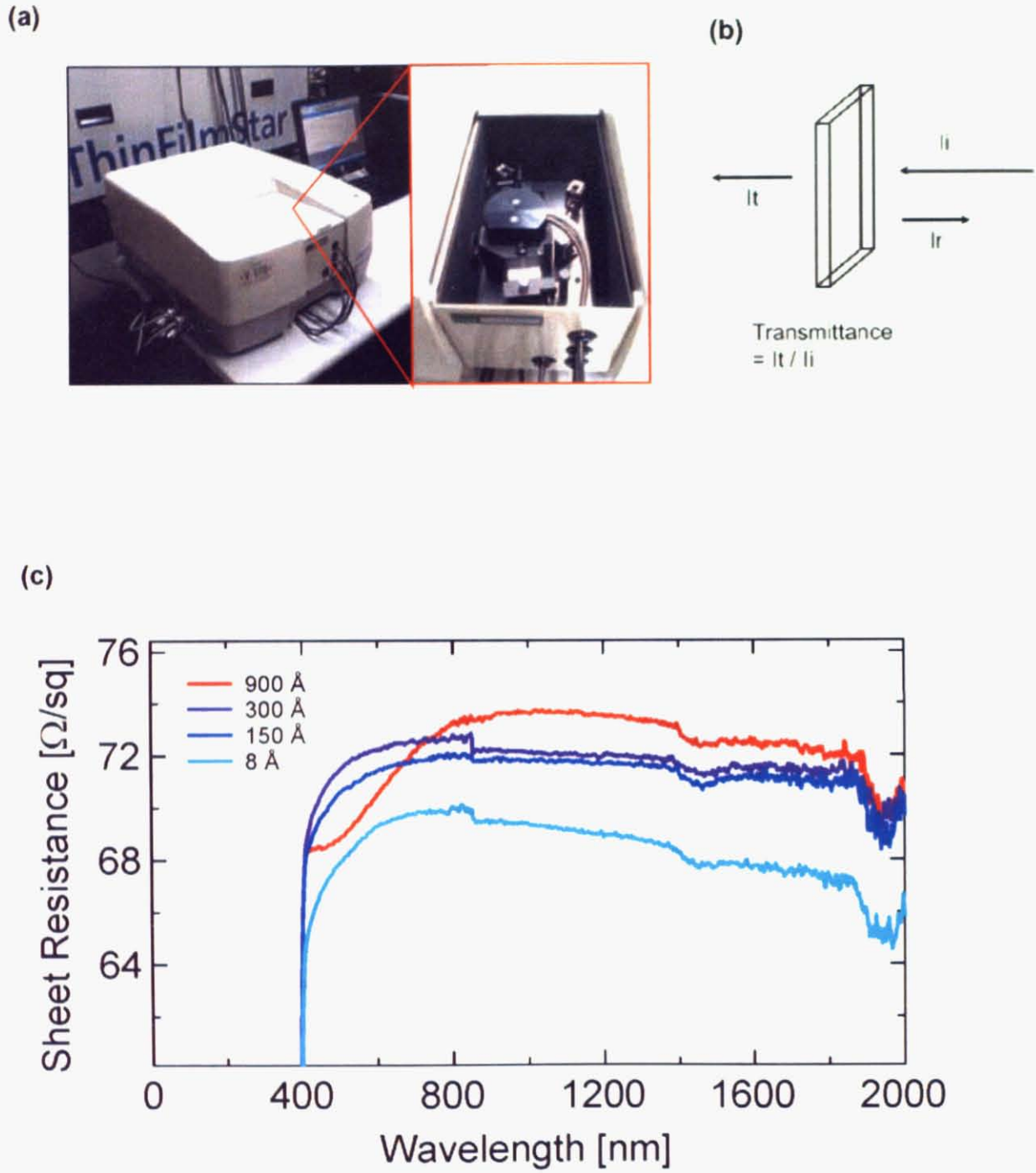

Fig.2-5-4

(a) A picture of the JASCO V570 UV-VIS-NIR spectrometer. (b) Schematic view of the transmittance measurement. The intensity of the incident light is Ii, the transmitted intensity is It and the reflected intensity is Ir. (c) Wavelength dependence of transmittance of annealed $LaTiO_3$ films.

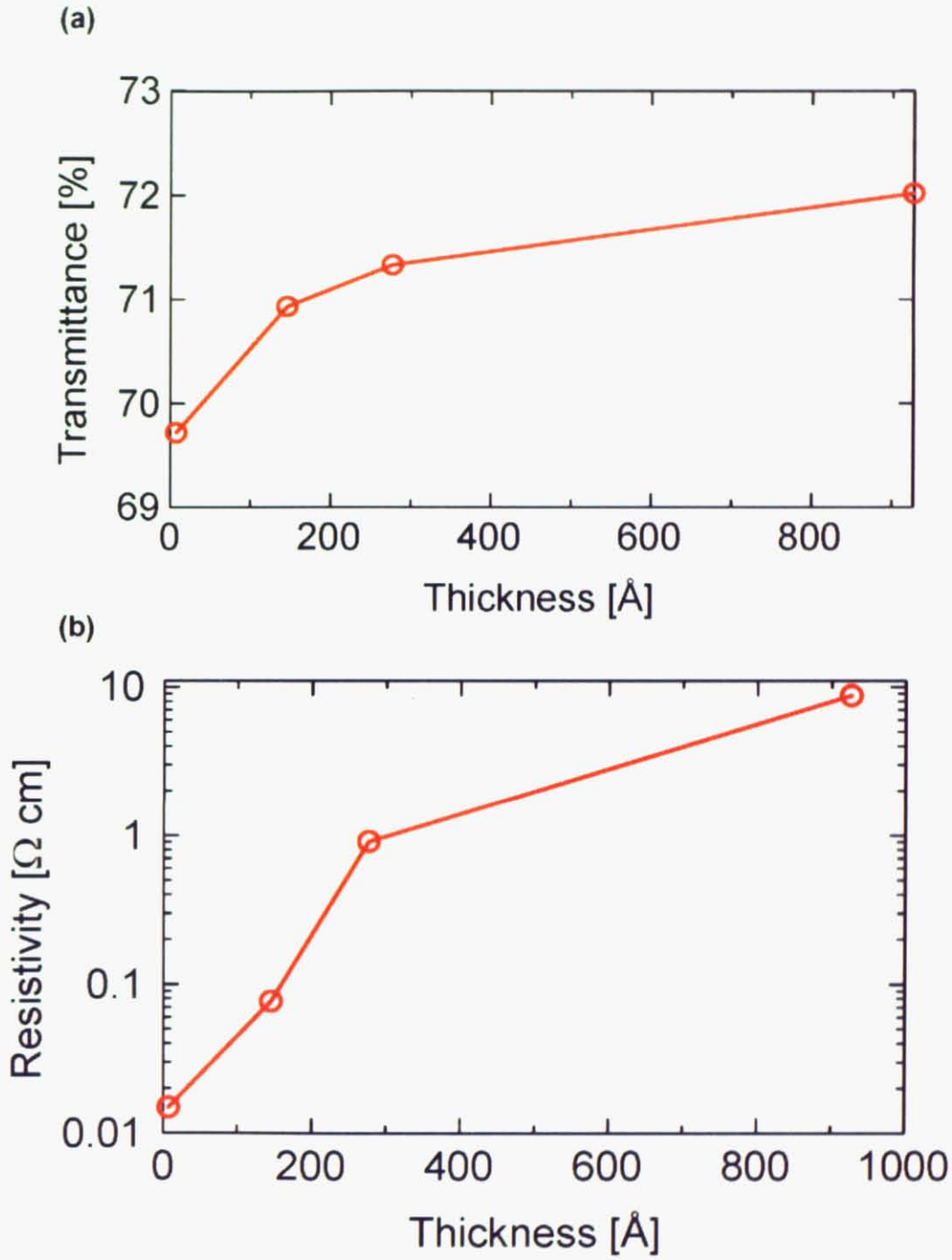

Fig.2-5-5

(a) Thickness dependence of transmittance of annealed $LaTiO_3$ films measured at a wavelength of 1800 nm. (b) Thickness dependence of resistivity at room temperature of annealed $LaTiO_3$ film grown on $SrTiO_3$.

References

[i] O. N. Tufte et al., Phys. Rev., **155**, 796 (1967)
[ii] A. Ohtomo et al., Appl. Phys. Lett., **80**, 3922 (2002)